Journal of Complex Networks (2020) **5**, Advance Access Publication on 4 November 2019,
Issue Publication on 1 February 2021
doi: 10.1093/comnet/cnz037

Random-graph models and characterization of granular networks

SILVIA NAUER
Department of Physics, Institute for Theoretical Physics, ETH Zurich, 8093 Zurich, Switzerland

LUCAS BÖTTCHER†
Department of Physics, Institute for Theoretical Physics, ETH Zurich, 8093 Zurich, Switzerland and Department of Management, Technology, and Economics, Center of Economic Research, ETH Zurich, 8092 Zurich, Switzerland
†Corresponding author. Email: lucasb@ethz.ch

AND

MASON A. PORTER
Department of Mathematics, University of California, Los Angeles, CA 90095, USA

Edited by: Ernesto Estrada

[Received on 31 July 2019; editorial decision on 7 September 2019; accepted on 10 September 2019]

Various approaches and measures from network analysis have been applied to granular and particulate networks to gain insights into their structural, transport, failure-propagation and other systems-level properties. In this article, we examine a variety of common network measures and study their ability to characterize various two-dimensional and three-dimensional spatial random-graph models and empirical two-dimensional granular networks. We identify network measures that are able to distinguish between physically plausible and unphysical spatial network models. Our results also suggest that there are significant differences in the distributions of certain network measures in two and three dimensions, hinting at important differences that we also expect to arise in experimental granular networks.

Keywords: random-graph models; granular networks; spatial networks.

1. Introduction

Various tools from network analysis have yielded insights into transport, failure mechanisms and other system-level properties of granular networks, which are typically constructed by interpreting the particles of the underlying packings as nodes and interpreting their contacts as edges [1–4]. Network analysis may help lead to better understanding and the ability to control fracture processes, design new materials and assess structural degradation in various engineering applications [5–7]. Researchers have employed continuum [5] and particle-level [7, 8] descriptions to study granular materials [9, 10], but neither framework is designed to study intermediate-scale organization, which is important for understanding and characterizing granular packings [2, 11].

In studies of granular and particulate networks, it is not clear which network measures are most suitable for distinguishing between physical granular networks and randomly embedded and overlapping particle systems. To take advantage of methods of network analysis, it is necessary to identify appropriate network measures to best highlight the distinctions between different structures [12]. Building on ideas from Ref. [13], we compute a variety of common network diagnostics and apply them to several spatial

network models and empirical granular networks in two and three dimensions. We identify measures that are able to distinguish between the network characteristics of physical and unphysical spatial networks that we construct from random particle systems. We test the convergence properties of our results by considering large ensembles of granular networks. Our results are useful both for the study of granular networks and because they help provide a roadmap for the development of random-graph models for studying spatially-embedded networks (such as transportation, communication and vascular systems). As has also been demonstrated in applications like sensor systems [14, 15], incorporating a small amount of physics into models such as random geometric graphs (RGGs) can provide important insights into the structure of such systems [12].

Our article proceeds as follows. In Section 2, we describe the network measures that we use in our investigation of spatial random graphs and granular networks. In Section 3, we present several models of both unphysical and physical granular networks. The network structures range from RGGs to physically plausible contact networks. To ensure comparability of our results with properties of real granular networks, we also apply our network measures to empirical granular network structures, and we generate our synthetic networks according to empirically observed edge densities. We thereby examine if certain network measures are able to distinguish between clearly unphysical (i.e., overlapping) granular packings and ones that are potentially physically plausible. In Section 4, we compare the distributions of the network diagnostics on the various networks. We also examine the convergence properties of the examined network diagnostics by computing them for ensembles of large networks. In Section 5, we conclude our study and discuss our results.

2. Network diagnostics

The structure of a network depends fundamentally on the processes and interactions that define it [16]. Many diagnostics have been developed to study and characterize networks, and we seek to use some of them to study granular networks and examine connections between network and particulate systems.

Consider a graph (i.e., network) $G(V, E)$, where V is a set of nodes and E is a set of edges. For each node $v \in V$, the degree $\deg(v)$ is the number of edges that are attached to v. For each node pair $\langle s, t\rangle \in V$, let $d_{\min}(s, t)$ denote a shortest path between s and t. We use σ_{st} to denote the number of shortest paths in a graph from s to t. The number of shortest paths from s to t that traverse $v \in V$ is $\sigma_{st}(v)$, and $\sigma_{st}(e)$ denotes the number of shortest paths from s to t that traverse an edge $e \in E$. We let $T(G)$ denote the number of triangles (i.e., a set of three nodes with an edge between each pair of nodes) in a network. We denote the number of triangles that include a node $v \in V$ by $T(G; v)$. We count each triangle three times when computing the number of triangles in a graph G.

All of the networks that we consider are unweighted and undirected, and we discuss several ways for characterizing them in the following paragraphs. To compute the values of these diagnostics, we use the Python library NetworkX. See Ref. [17] for a detailed documentation.

Many of the diagnostics depend on the number of nodes in a network. Therefore, in each of the models that we study, we set the number of nodes to be equal to the number in the experimental data. This allows us to compare the diagnostics in our models and the empirical granular networks.

2.1 *Edge density.*

The edge density (or sometimes just 'density') of an undirected network is [16]

$$\rho = \frac{2|E|}{|V|(|V| - 1)}, \tag{1}$$

where $|E|$ is the number of edges and $|V|$ is the number of nodes. We use edge density as a reference measure for the construction of our networks. To compare the results of different network models, we first make sure that their edge densities are the same. From this density and the number of nodes, we derive the number of edges, which we use in our generation of random graphs.

2.2 *Geodesic node betweenness.*

The geodesic node betweenness centrality c_B of a node v is the sum (over all node pairs $\langle s, t\rangle$ in a network) of the number of shortest paths from s to t that traverse v divided by the total number of shortest paths from s to t [16]. Including a normalization factor, we write geodesic node betweenness centrality as

$$c_B(v) = \sum_{\langle s,t\rangle \in V} \frac{\sigma_{st}(v)}{\sigma_{st}} \underbrace{\frac{2}{(|V|-1)(|V|-2)}}_{\text{normalization factor}} . \tag{2}$$

Note that $\sigma_{st} = 1$ if $s = t$ and that $\sigma_{st}(v) = 0$ if $v \in \{s, t\}$. We define a network's geodesic node betweenness

$$C_B(G) = \frac{1}{|V|} \sum_{v \in V} c_B(v) \tag{3}$$

as the mean of the geodesic node betweenness centralities over all nodes in a network.

A large geodesic betweenness centrality $c_B(v)$ suggests that many shortest paths traverse a particular node. This may in turn suggest that such a node is relevant for transportation processes or failure-propagation mechanisms in granular networks [1–4].

2.3 *Geodesic edge betweenness.*

We can also calculate a geodesic betweenness centrality for edges [18]:

$$c_B(e) = \sum_{\langle s,t\rangle \in V} \frac{\sigma_{st}(e)}{\sigma_{st}} \underbrace{\frac{2}{|V|(|V|-1)}}_{\text{normalization factor}} . \tag{4}$$

Note that $\sigma_{st}(e) = 0$ if $s = t$, and we again take $\sigma_{st} = 1$ when $s = t$. Based on Eq. (4), the geodesic edge betweenness of a network is

$$C_B(G) = \frac{1}{|E|} \sum_{e \in E} c_B(e) . \tag{5}$$

2.4 *Clustering coefficient.*

The local clustering coefficient $c(v)$ of a node v with degree $\deg(v) \geq 2$ is the number of triangles that include that node divided by the number of all possible triangles that could include v (i.e., the connected triples) [16]. That is,

$$c(v) = \frac{2T(G; v)}{\deg(v)(\deg(v) - 1)} . \tag{6}$$

If the degree of a node is 0 or 1, the corresponding clustering coefficient of that node is 0. The mean local clustering coefficient of a network is

$$c(G) = \frac{1}{|V|} \sum_{v \in V} c(v) \,. \tag{7}$$

2.5 *Transitivity.*

Transitivity is the number of triangles in a network divided by the number of possible triangles [16]:

$$\text{Transitivity} = \frac{T(G)}{\text{number of possible triangles in } G} \,. \tag{8}$$

Based on the definition of mean local clustering coefficient and transitivity, we see that these two measures are closely related.

2.6 *Degree assortativity.*

Degree assortativity is a measure to quantify the correlation between the degree of a node v and the degrees of its neighbours [16]. Larger values of degree assortativity entail greater similarity in the degrees of neighbouring nodes. We compute degree assortativity by calculating a Pearson correlation coefficient, whose values lie in the interval $[-1, 1]$ [19]. A value of 1 indicates a network with perfect degree assortativity, a value of 0 corresponds to a non-assortative network and a value of -1 indicates perfect degree disassortativity.

2.7 *Global efficiency.*

The efficiency $E(u, v)$ of a node pair $\langle u, v \rangle$ is the inverse of the shortest-path length between these two nodes [20]. That is,

$$E(u, v) = \frac{1}{d_{\min}(u, v)} \,. \tag{9}$$

Global efficiency is the mean of the efficiencies over all pairs of nodes in a network:

$$E_{\text{glob}}(G) = \frac{1}{|\{\langle u, v \rangle \in V\}|} \sum_{\langle u,v \rangle \in V} E(u, v) \,. \tag{10}$$

2.8 *Local efficiency.*

The local efficiency [20] of a node v is

$$E_{\text{loc}}(v) = \frac{1}{|\langle u, w \rangle \in \Gamma(v)|} \sum_{\langle u,w \rangle \in \Gamma(v)} E(u, w) \,, \tag{11}$$

where $\Gamma(v)$ denotes the neighbourhood of v. The local efficiency

$$E_{\mathrm{loc}}(G) = \frac{1}{|V|} \sum_{v \in V} E_{\mathrm{loc}}(v) \tag{12}$$

of a network is the mean of the local efficiencies over all nodes of the network.

2.9 *Mean shortest-path length in the largest connected component (LCC).*

The mean shortest-path length over all node pairs $\langle u, v \rangle$ of a largest connected component (LCC) $C_{\max}$ of a network is

$$\bar{d}_{\min} = \frac{1}{|\{\langle u, v \rangle \in C_{\max}\}|} \sum_{\langle u,v \rangle \in C_{\max}} d_{\min}(u, v)\,. \tag{13}$$

2.10 *Weighted mean shortest-path length.*

The weighted mean shortest-path length $\bar{d}^{w}_{\min}$ is the weighted arithmetic mean of the mean shortest-path lengths $\bar{d}_{\min}(G_C)$ that we compute for connected components G_C of a graph. We use the number of nodes in each component as a weight, so

$$\bar{d}^{w}_{\min} = \frac{1}{|V|} \sum_{G_C \in G} \bar{d}_{\min}(G_C)\, |G_C|\,, \tag{14}$$

where $|G_C|$ denotes the number of nodes in the considered connected component.

2.11 *Maximized modularity.*

Subgraphs of a network G are often called 'communities' in the context of dense sets of nodes that are connected sparsely to other dense sets of nodes [21, 22]. Given a set of communities of a network G, the modularity $Q \in [-1, 1]$ measures the density of edges (adjusted for edge weights) inside communities compared with that between communities [23]. For an unweighted graph, the modularity Q of a partition of a graph G is

$$Q = \frac{1}{2|E|} \sum_{\langle u,v \rangle \in G} \left[A_{uv} - \frac{\deg(u)\deg(v)}{2|E|} \right] \delta(g_u, g_v)\,, \tag{15}$$

where A is the adjacency matrix of the network, δ is the Kronecker delta and g_u denotes the community that includes node u.

We maximize modularity by applying the locally greedy Louvain method for community detection [23]. Maximized modularity measures how well one can partition a network into disjoint communities [22].

2.12 *Subgraph centrality.*

For a node v and an adjacency matrix A associated with a graph G, the subgraph centrality [24]

$$S(v) = \sum_{k=0}^{\infty} \frac{\left(A^k\right)_{vv}}{k!} \tag{16}$$

is the sum of weighted closed walks (of all lengths) that start and end at node v. Instead of weighting each term with $1/k!$, one can also make other choices for the weights. The (u, v)th element of A^k represents the number of paths of length k from node u to node v. The mean subgraph centrality of a network G is

$$S(G) = \frac{1}{|V|} \sum_{v \in V} S(v) \,. \tag{17}$$

2.13 *Communicability.*

The communicability [25]

$$C_{\mathrm{com}}(u, v) = \sum_{k=0}^{\infty} \frac{(A^k)_{uv}}{k!} \tag{18}$$

between nodes u and v measures the number of closed walks between nodes u and v.

The communicability of a network G is the mean of the communicabilities between all pairs of nodes in the network:

$$C_{\mathrm{com}}(G) = \frac{1}{|\{\langle u, v\rangle \in V\}|} \sum_{\langle u,v\rangle \in V} C_{\mathrm{com}}(u, v) \,. \tag{19}$$

3. Random-graph models of granular networks

As baselines to compare to empirical granular networks, we consider various models of spatial networks in two and three dimensions. We start with a standard RGG, which is an unphysical model, and then we examine some more realistic models (such as force-modified RGGs). After discussing these models in two dimensions, we also examine some models in three dimensions. The reason for studying different models, ranging from unphysical ones to more physical ones, is that we aim to identify diagnostics that are able to capture properties of realistic granular networks, which one constructs from non-overlapping particles that interact with each other [13]. The model networks also allow us to analyse the convergence properties of network measures, because we can generate large numbers of different network configurations and examine how they behave when they have progressively more nodes. We also apply our network measures to two-dimensional empirical granular networks and use the empirically determined edge densities as input for our granular network models in two dimensions. Given a specific edge density, we perform all of the computations for the same configuration as in the experiments (see Section 3.5). Specifically, the empirical granular systems are confined by a two-dimensional box with dimensions 290 mm $\times$ 380 mm and have a mean of 1122 particles. To study models of three-dimensional materials, we examine model networks with 1122 particles in a box with dimensions 102 mm $\times$ 102 mm $\times$ 102 mm.

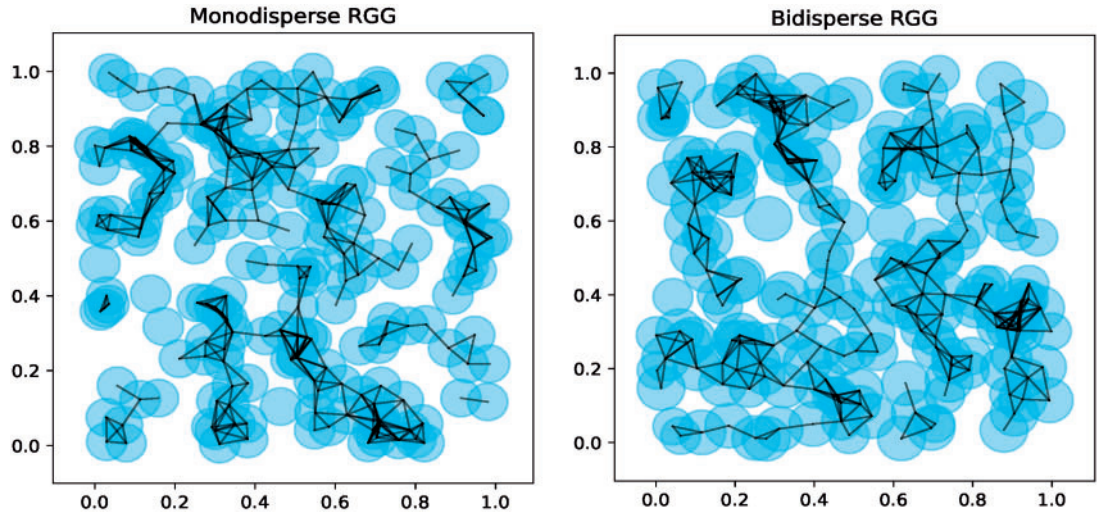

FIG. 1. (Left) Monodisperse and (right) bidisperse RGG in the unit square. The monodisperse RGG has $n = 200$ nodes, particles of radius $r = 0.05$ and a distance parameter of $R \approx 0.0428$. The bidisperse RGG has $n = 200$ nodes, particles of radius $r_1 = 0.05$ and $r_2 = 0.06$ (there are 92 particles of radius r_1 and 108 particles of radius r_2) and a distance parameter of $R \approx 0.7770$. In the bidisperse case, we generate a uniformly distributed random number $\epsilon \sim \mathcal{U}(0, 1)$ for each particle. If $\epsilon < 0.5$, we set the particle radius to r_1; otherwise, we set it to r_2.

3.1 *Random geometric graphs*

As a first, overly simplistic model of a granular system, we consider a monodisperse random geometric graph (RGG). In this model, we place n particles (represented by nodes) of the same radius r uniformly at random in a box. The nodes are adjacent if the distance between them is smaller than $2R$, where we choose the parameter R based on the edge density that matches an empirical granular network that we will study later (see Section 3.5). Because of the possibility of multiple overlapping particles, this monodisperse RGG is not a good model of a physical granular system. We also consider a bidisperse RGG. In this model, the particles can have two different radii, r_1 and r_2; nodes i and j are adjacent to each other if the distance between them is smaller than $R\left(r_i + r_j\right)$. For each particle, we generate a uniformly distributed random number $\epsilon \sim \mathcal{U}(0, 1)$. If $\epsilon < 0.5$, we set the particle radius to r_1; otherwise, we set it to r_2. We use the same procedure for all bidisperse models in this article. We want 50%, on average, of particles to have radius r_1 to facilitate our comparison with the employed experimental granular network data (see Section 3.5). As in the monodisperse case, we place particles uniformly at random. We again need to choose R to match a desired edge density. We show examples of both a monodisperse and a bidisperse RGG in Fig. 1.

The parameters in our computations are $n = 1122$ nodes, a radius of $r = 4.5$ and a distance parameter of $R \approx 5.69$ for the monodisperse RGG and $n = 1122$, $r_1 = 4.5$, $r_2 = 5.5$ and $R \approx 1.13$ for the bidisperse RGG.

3.2 *Proximity-modified RGGs*

To compensate for some of the overlaps between particles in an RGG, we now define a proximity measure p that describes the distance between each point (x, y) and its nearest particle(s). Initially, the system is

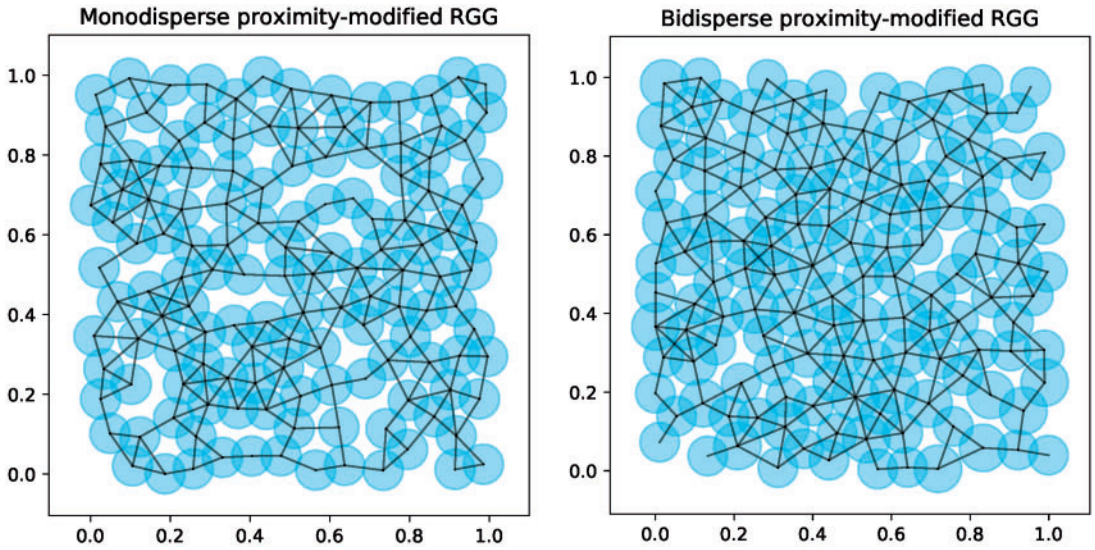

FIG. 2. Monodisperse and bidisperse proximity-modified RGGs in the unit square. The parameters are $n = 135$, $r = 0.05$, $\alpha = 0.7$ and $R \approx 0.0588$ for the monodisperse example and $n = 135$, $r_1 = 0.05$, $r_2 = 0.06$ (there are 90 particles of radius r_1 and 45 particles of radius r_2), $\alpha = 0.7$ and $R \approx 1.1020$ for the bidisperse example. The parameter α enforces a maximum particle density in a given region. In the bidisperse case, we generate a uniformly distributed random number $\epsilon \sim \mathcal{U}(0, 1)$ for each particle. If $\epsilon < 0.5$, we set the particle radius to r_1; otherwise, we set it to r_2.

empty. We then place each particle as follows. For each integer $k \in \{1, \ldots, n\}$, we place particle k, which has a radius of r_k, in the box. To do this, we choose a position (x_k, y_k) in the box uniformly at random, and we place the particle with probability

$$P(p_k) = \begin{cases} 0\,, & \text{for } p_k < 2\alpha r_k\,, \\ 1\,, & \text{for } p_k \geq 2\alpha r_k\,, \end{cases} \tag{20}$$

where p_k is the proximity measure for the position (x_k, y_k) and $\alpha \in [0, 1]$ is a parameter that enforces a maximum particle density in a given region. We use this procedure for both monodisperse ($r_k = r$) and bidisperse ($r_k \in \{r_1, r_2\}$) particle configurations. We generate the edges in the same way as in the bidisperse RGG model.

In Fig. 2, we show examples of monodisperse and bidisperse proximity-modified RGGs. Based on the depicted configurations, we see that the proximity-modified RGGs have fewer overlaps than the standard RGGs. However, overlaps are still present, so the model does not describe a physical granular network.

For our computations, we use the parameters $n = 1122$, $r = 4.5$, $\alpha = 0.75$ and $R \approx 1.39$ for the monodisperse case and $n = 1122$, $r_1 = 4.5$, $r_2 = 5.5$, $\alpha = 0.75$ and $R \approx 1.24$ for the bidisperse case. In the bidisperse case, we generate a uniformly distributed random number $\epsilon \sim \mathcal{U}(0, 1)$ for each particle. If $\epsilon < 0.5$, we set the particle radius to r_1; otherwise, we set it to r_2.

3.3 *Force-modified RGGs*

To obtain a network whose characteristics better resemble those of a physical granular packing, we now apply a different modification to an RGG. Initially, we start from an RGG configuration. Subsequently, for each particle k, we suppose that particles interact via a Hertzian-like contact [26] and compute the force

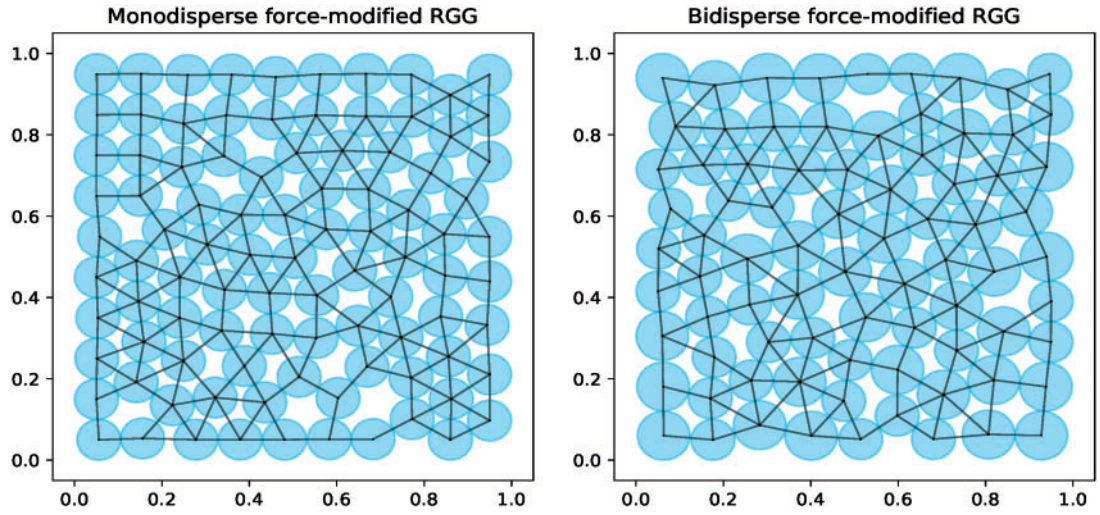

FIG. 3. Monodisperse and bidisperse force-modified RGGs in the unit square. We use the parameters $n = 95$, $r = 0.05$, $\beta = 0.5$ and $R \approx 0.0615$ for the monodisperse case and $n = 80$, $r_1 = 0.05$, $r_2 = 0.06$ (there are 41 particles of radius r_1 and 39 particles of radius r_2), $\beta = 0.5$ and $R \approx 1.2280$ for the bidisperse case. To generate these configurations, we update the positions $\mathbf{x}_k$ of all particles 700 times using $\mathbf{x}_k \to \mathbf{x}_k + \mathbf{d}_k$. The displacement $\mathbf{d}_k$ is proportional to the force $\mathbf{f}_k$ (see Eq. (21)), and the parameter β gives the exponent in the force law. In the bidisperse case, we generate a uniformly distributed random number $\epsilon \sim \mathcal{U}(0, 1)$ for each particle. If $\epsilon < 0.5$, we set the particle radius to r_1; otherwise, we set it to r_2.

$\mathbf{f}_k$ that acts on particle k from overlaps with other particles. After computing $\mathbf{f}_k$ for all k, we update the corresponding particle locations $\mathbf{x}_k$ according to $\mathbf{x}_k \to \mathbf{x}_k + \mathbf{d}_k$, with $\mathbf{d}_k = \varepsilon \mathbf{f}_k$. We repeat this process until the particles no longer overlap (see Appendix A). One can use the parameter ε to rescale the displacements $\mathbf{d}_k$, which may be too large and potentially lead to new overlaps between particles if we do not reduce them. For a box with dimensions $L_x \times L_y$ and according to the Hertzian-like contact, the force on particle k is [26, 27]

$$\begin{aligned}\mathbf{f}_k = \sum_{l \neq k} \left\{ \left[\frac{1}{2}(r_k + r_l) - \frac{1}{2}|\mathbf{x}_k - \mathbf{x}_l| \right]_+^{\beta} \frac{\mathbf{x}_k - \mathbf{x}_l}{|\mathbf{x}_k - \mathbf{x}_l|} \right\} \\ + [r_k - x_k]_+^{\beta} \hat{\mathbf{x}} - [r_k + x_k - L_x]_+^{\beta} \hat{\mathbf{x}} + \left[r_k - y_k\right]_+^{\beta} \hat{\mathbf{y}} - \left[r_k + y_k - L_y\right]_+^{\beta} \hat{\mathbf{y}}\,,\end{aligned} \tag{21}$$

where the exponent β (which is $\beta = 3/2$ in classical Hertzian theory but was estimated to be $\beta = 5/4$ for the two-dimensional granular material in Ref. [26]) describes the interaction strength between particles. The vectors $\hat{\mathbf{x}}$ and $\hat{\mathbf{y}}$ are the unit vectors in the x and y directions, respectively. Forces occur only between overlapping particles or between a particle and the boundary of the box if they are in contact. Therefore, the bracket $[x]_+$ in Eq. (21) is

$$[x]_+ = \begin{cases} x\,, & \text{for } x > 0\,, \\ 0\,, & \text{for } x \leq 0\,. \end{cases} \tag{22}$$

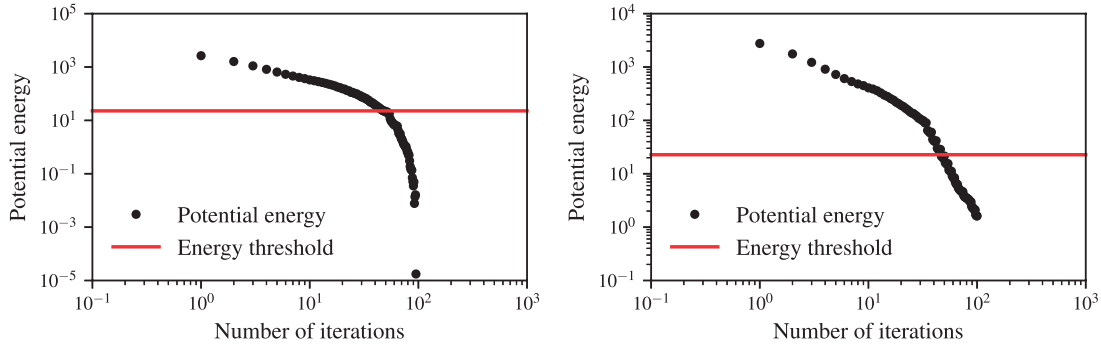

FIG. 4. Energy convergence for the monodisperse force-modified RGG model. We generate RGGs using the parameter values $n = 1122$, $r = 4.5$, $\beta = 0.5$ and $R \approx 1.29$ for a box with dimensions $L_x = 290$ and $L_y = 380$. For both of our examples, we update the positions $\mathbf{x}_k$ of all particles 100 times using $\mathbf{x}_k \to \mathbf{x}_k + \mathbf{d}_k$. The displacement $\mathbf{d}_k$ is proportional to the force $\mathbf{f}_k$ (see Eq. (21)). The left panel shows an example in which the energy approaches 0, and the right panel shows an example in which the energy does not approach 0 but is smaller than some threshold (which we indicate with the solid red line) that we choose such that there are no visible overlaps between particles (see Appendix A).

The potential energy that corresponds to (21) is

$$V = \sum_k \sum_{l \neq k} \left\{ \left[\frac{1}{2}(r_k + r_l) - \frac{1}{2}|\mathbf{x}_k - \mathbf{x}_l| \right]_+^{\beta+1} \right\} + [r_k - x_k]_+^{\beta+1} - [r_k + x_k - L_x]_+^{\beta+1} + \left[r_k - y_k\right]_+^{\beta+1} - \left[r_k + y_k - L_y\right]_+^{\beta+1} . \tag{23}$$

The first term of Eqs. (21) and (23) accounts for overlaps between particles, and the other terms take into account the left, right, bottom and top boundaries of the box. We generate the edges in this model as we did for bidisperse RGGs. We show examples of monodisperse and bidisperse force-modified RGGs in Fig. 3. In this figure, it appears (based on visual inspection) that particles do not overlap anymore. At least visually, they more closely resemble real granular networks than is the case for the standard RGGs and the proximity-modified RGGs.

To attempt to ensure that our final configurations are free of overlaps, we monitor their energy. If the energy is 0, there are no overlaps, so we stop updating locations when we cannot distinguish the energy from 0. However, in some cases, the energy does not approach 0, because some particles are locally jammed [28]. In such cases, we accept a configuration if its energy is smaller than the energy of a system in which each particle k has an overlap distance of no more than $r_k/200$ with all of its neighbours. In Fig. 4, we show the monitored energy for two cases of a monodisperse force-modified RGG. A situation in which many particles overlap with their neighbours is unlikely to occur. Instead, there are often some particles that overlap with one or two neighbours with a large fraction of their areas. To avoid large overlaps, we also check for every configuration that each particle k does not have an overlap distance with a neighbour that is larger than $r_k/15$. See Appendix A for details.

The parameters in our computations are $n = 1122$, $r = 4.5$, $\beta = 0.5$, $L_x = 290$, $L_y = 380$ and $R \approx 1.2900$ for the monodisperse case. For the bidisperse case, they are $n = 1122$, $r_1 = 4.5$, $r_2 = 5.5$, $\beta = 0.5$, $L_x = 290$, $L_y = 380$ and $R \approx 1.0850$. To generate these configurations, we perform 100 iterations for the monodisperse case and 400 iterations for the bidisperse one. As in the standard RGG

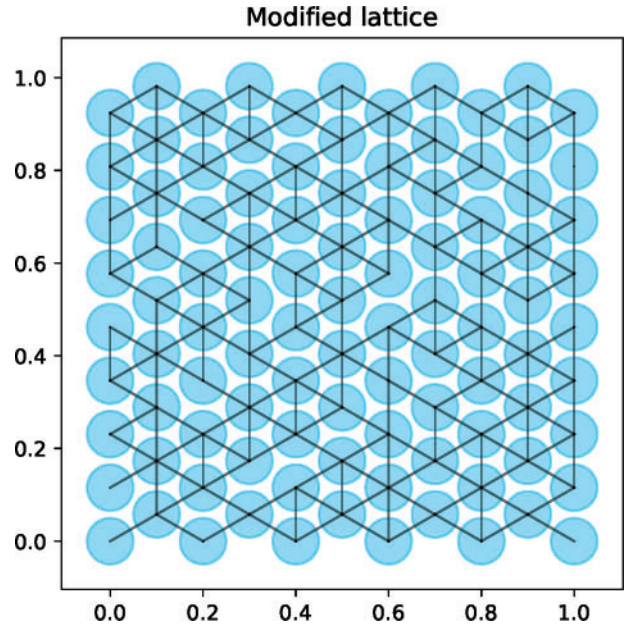

FIG. 5. Modified lattice in the unit square. We consider 99 particles of radius $r = 0.05$ and a removal fraction of $\mu \approx 0.1870$.

model, 50% of the particles, on average, in the bidisperse case have a radius of r_1; the others have a radius of r_2.

3.4 *Modified lattice*

We also consider a modified lattice. In this model, we modify a hexagonal lattice of particles of the same radii by removing a fraction μ of edges uniformly at random to match a certain edge density. We show an example of a modified lattice in Fig. 5. In our computations, we use a total of 1020 particles, with $r = 4.5$ and $\mu \approx 0.26$.

3.5 *Experimental data*

To compare our model networks with real granular networks, we extract granular networks from experimental data [29]. Henceforth, when we write 'experimental data', we mean data from a bidisperse granular system with radii $r_1 = 4.5$ mm and $r_2 = 5.5$ mm in a two-dimensional box with side lengths $L_1 = 290$ mm and $L_2 = 380$ mm. The employed experimental data set consists of 17 different configurations of granular networks. We compute the diagnostics of Section 2 for these 17 cases, and we present the corresponding diagnostic values in Appendix B. On average, the number of particles in the experimental configurations is 1122, and 49.2% of the particles have a radius of r_1. Therefore, we use 1122 particles in our model networks to facilitate comparisons between our models and the experimental data. For the bidisperse network models, we generate a uniformly distributed random number $\epsilon \sim \mathcal{U}(0, 1)$. If $\epsilon < 0.5$, we set the particle radius to r_1; otherwise, we set it to r_2. We consider bidisperse packings, as we wish to avoid the crystallization of monodisperse packings. We show an example of the experimental setup in Fig. 6. To obtain such a configuration, Ref. [29] placed about 1000 particles (which were cut from Vishay PSM-4

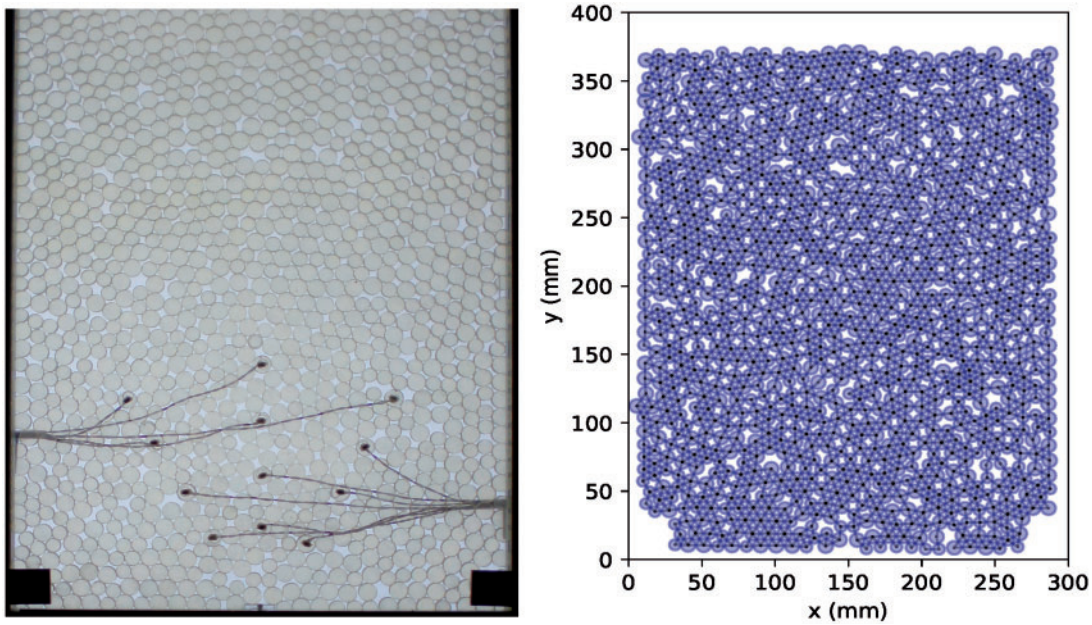

FIG. 6. Experimental granular network. The particles have radii $r_1 = 4.5$ mm and $r_2 = 5.5$ mm, and the box has sides of lengths $L_1 = 290$ mm and $L_2 = 380$ mm. In the left panel, we show the experimental setup; in the right panel, we show the corresponding extracted granular network. We use data from Ref. [29].

photoelastic material) into a container with an open top, such that the particles were confined only by gravity.

3.6 *Models in three dimensions*

As with the two-dimensional examples, we calculate the network diagnostics of Section 2 for three-dimensional granular networks. In this section, we briefly discuss extensions of the previously-discussed models to three dimensions. The standard RGGs do not require any special modification for the generation of the configurations, although the underlying box is now in three dimensions. We show examples of three dimensions monodisperse and bidisperse RGGs in the top panels of Fig. 7. As in the two-dimensional RGGs, we observe that the particles overlap, so the model is not physical. Our parameters for these models are $n = 1122$, $r = 4.5$ and $R \approx 6.0750$ for the monodisperse case and $n = 1122$, $r_1 = 4.5$, $r_2 = 5.5$ and $R \approx 1.1950$ for the bidisperse case. As in the two-dimensional models, 50% of the particles in our three-dimensional models have radius r_1 on average and the others have radius r_2.

It is also straightforward to extend the proximity-modified RGGs to three dimensions. We show examples of three-dimensional monodisperse and bidisperse proximity-modified RGGs in the bottom panels of Fig. 7. We see that the particles overlap less than for the unmodified three-dimensional RGGs, but they still overlap. To obtain these configurations, we use the parameters $n = 1122$, $r = 4.5$, $\alpha = 0.75$ and $R \approx 1.4200$ for the monodisperse case and $n = 1122$, $r_1 = 4.5$, $r_2 = 5.5$, $\alpha = 0.75$ and $R \approx 1.4385$ for the bidisperse case.

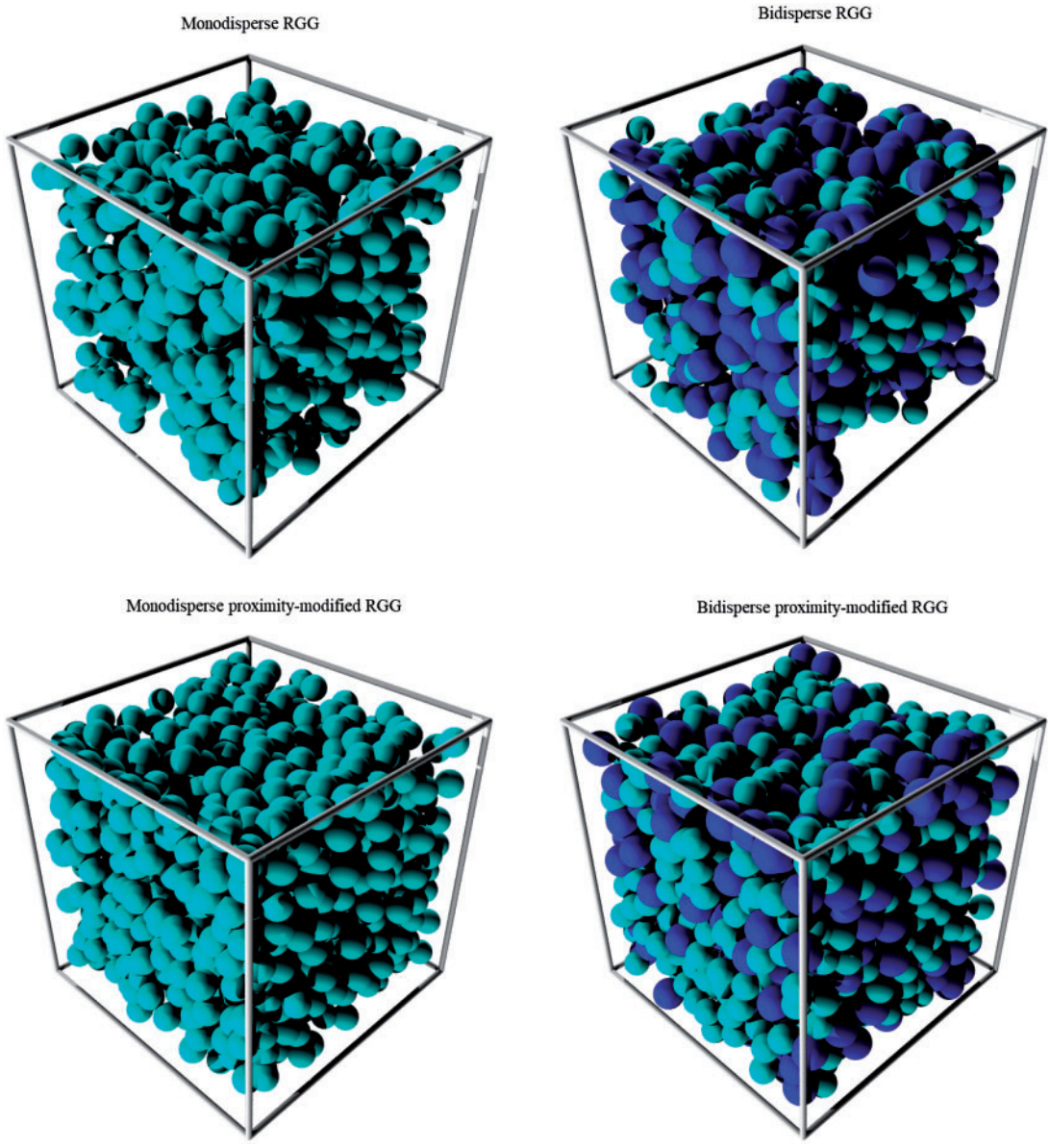

FIG. 7. Three-dimensional RGGs and proximity-modified RGGs. For the standard RGGs, the parameters are $n = 1122$, $r = 4.5$ and $R \approx 6.0750$ for the monodisperse case and $n = 1122$, $r_1 = 4.5$, $r_2 = 5.5$ and $R \approx 1.1950$ for the bidisperse case. For the proximity-modified RGG models, the parameters are $n = 1122$, $r = 4.5$, $\alpha = 0.75$ and $R \approx 1.4200$ for the monodisperse case and $n = 1122$, $r_1 = 4.5$, $r_2 = 5.5$, $\alpha = 0.75$ and $R \approx 1.4385$ for the bidisperse case. In the bidisperse case, we generate a uniformly distributed random number $\epsilon \sim \mathcal{U}(0, 1)$ for each particle. If $\epsilon < 0.5$, we set the particle radius to r_1; otherwise, we set it to r_2. In all four examples, we consider a box with dimensions $L_x \times L_y \times L_z = 102 \times 102 \times 102$.

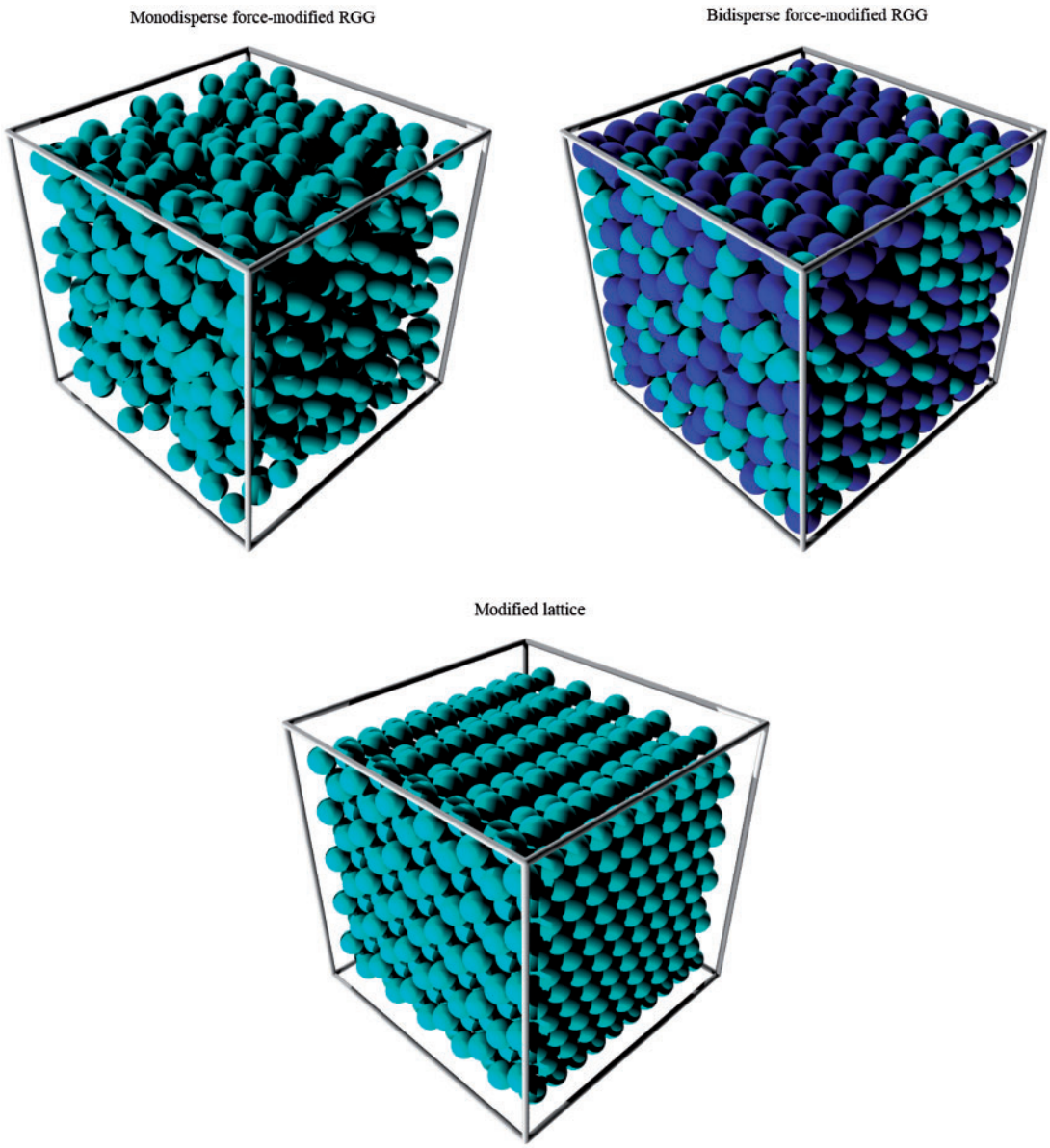

FIG. 8. Three-dimensional force-modified RGG and modified lattice models. For the force-modified RGG models, the parameters are $n = 1122$, $r = 4.5$, $\beta = 0.5$ and $R \approx 1.4080$ for the monodisperse case and $n = 1122$, $r_1 = 4.5$, $r_2 = 5.5$, $\beta = 0.5$ and $R \approx 1.2600$ for the bidisperse case. To generate these configurations, we update the positions $\mathbf{x}_k$ of all particles 100 times for the monodisperse case and 400 times for the bidisperse case according to $\mathbf{x}_k \to \mathbf{x}_k + \mathbf{d}_k$, where the displacement $\mathbf{d}_k$ is proportional to the force $\mathbf{f}_k$ (see Eq. (24)). For the modified lattice, we arrange 1100 particles of radius $r = 4.5$ in a hexagonal close packing and we set $\mu \approx 0.4950$. In the bidisperse case, we generate a uniformly distributed random number $\epsilon \sim \mathcal{U}(0, 1)$ for each particle. If $\epsilon < 0.5$, we set the particle radius to r_1; otherwise, we set it to r_2. In all cases, we consider a box with dimensions $L_x \times L_y \times L_z = 102 \times 102 \times 102$.

For the force-modified RGGs, we have to adapt Eqs. (21) and (23) to three dimensions. Equation (21) becomes

$$\begin{aligned}\mathbf{f}_k = \sum_{l\neq k}\Bigg\{&\left[\frac{1}{2}(r_k+r_l)-\frac{1}{2}|\mathbf{x}_k-\mathbf{x}_l|\right]_+^{\beta}\frac{\mathbf{x}_k-\mathbf{x}_l}{|\mathbf{x}_k-\mathbf{x}_l|}\Bigg\}\\ &+[r_k-x_k]_+^{\beta}\,\hat{\mathbf{x}}-[r_k+x_k-L_x]_+^{\beta}\,\hat{\mathbf{x}}+\left[r_k-y_k\right]_+^{\beta}\,\hat{\mathbf{y}}-\left[r_k+y_k-L_y\right]_+^{\beta}\,\hat{\mathbf{y}}\\ &+[r_k-z_k]_+^{\beta}\,\hat{\mathbf{z}}-[r_k+z_k-L_z]_+^{\beta}\,\hat{\mathbf{z}}\,,\end{aligned} \tag{24}$$

where $\hat{\mathbf{z}}$ denotes the unit vector in the z direction. Equation (23) becomes

$$\begin{aligned}V = \sum_k\sum_{l\neq k}\Bigg\{&\left[\frac{1}{2}(r_k+r_l)-\frac{1}{2}|\mathbf{x}_k-\mathbf{x}_l|\right]_+^{\beta+1}\Bigg\}\\ &+[r_k-x_k]_+^{\beta+1}-[r_k+x_k-L_x]_+^{\beta+1}+\left[r_k-y_k\right]_+^{\beta+1}-\left[r_k+y_k-L_y\right]_+^{\beta+1}\\ &+[r_k-z_k]_+^{\beta+1}-[r_k+z_k-L_z]_+^{\beta+1}\ .\end{aligned} \tag{25}$$

We show examples of three-dimensional force-modified RGGs in the top panels of Fig. 8. As in the two-dimensional case, we conclude based on visual inspection that they resemble real granular networks more closely than the other models. The parameters in our computations are $n = 1122$, $r = 4.5$, $\beta = 0.5$ and $R \approx 1.4080$ for the monodisperse case and $n = 1122$, $r_1 = 4.5$, $r_2 = 5.5$, $\beta = 0.5$ and $R \approx 1.2600$ for the bidisperse case. In both examples, we set $L_x = L_y = L_z = 102$. To generate these configurations, we perform 100 iterations for the monodisperse case and 400 iterations for the bidisperse one. We describe the energy thresholds for the three-dimensional force-modified RGGs in Appendix A.

We extend the modified lattice to three dimensions by considering spheres in a hexagonal close packing (HCP). An HCP consists of a series of two alternating layers of spherical particles, where each layer has a hexagonal arrangement. We create the edges in the same way as in the two-dimensional modified lattice. In the bottom panel of Fig. 8, we show an example of a three-dimensional modified lattice that consists of 1100 particles. The particles have a radius of $r = 4.5$, and we remove a fraction $\mu \approx 0.4950$ of the edges uniformly at random from the network.

4. Results

4.1 *Diagnostics for two-dimensional granular networks*

We first focus on the results of calculating the network diagnostics for the two-dimensional models from Section 3. We describe the convergence characteristics of all diagnostics and then discuss the distributions of several of them.

4.1.1 *Convergence characteristics* To monitor the convergence of the diagnostics, we generate 10 ensembles with different numbers of granular-network configurations. Specifically, ensemble m has 2^m networks (where $m \in \{0, \ldots, 9\}$), so there are 1023 networks in total. For each m, we compute the mean of the diagnostic values and normalize each value by the mean that we calculate for $m = 9$. Therefore, each of the mean diagnostic values approaches 1 for $m = 9$ (see Fig. 9). This procedure allows us to identify a reasonable number of networks such that the deviations of the mean diagnostic values are

sufficiently small in comparison to the values in the largest ensemble. We thereby study the convergence properties of the mean diagnostic values with respect to the values in the largest ensemble. Based on the data in Fig. 9, we see that the diagnostics behave differently in the different network models.

In the unmodified RGG models, some of the normalized mean diagnostics deviate more from 1 than in the other models. We observe this behaviour for geodesic node betweenness, geodesic edge betweenness, subgraph centrality and communicability. Because we place the particles in the RGGs uniformly at random, different configurations can differ substantially from each other. For example, in our computations, we observe that some configurations have local accumulations of particles; such outliers strongly influence the mean for ensembles with a small number of networks. By contrast, these outliers exert less influence for ensembles with many networks, so they have a smaller effect on those ensembles. For the aforementioned diagnostics, such particle accumulations in some samples lead to the zigzag behaviour in Fig. 9. In the other network models, this issue is less prominent, because local particle accumulations are suppressed by the proximity and force modifications. The larger deviations of the mean diagnostics in the unmodified RGG models are also reflected in their distributions (see Section 4.1.3). For the proximity-modified RGGs and the force-modified RGGs, the mean diagnostic values approach the values that we observe in the largest ensemble faster than in the unmodified RGG models. For the modified-lattice model, we observe that almost all mean diagnostic curves are constant; the only exception is degree assortativity. In this model, the only process that has any randomness is deleting edges from the initially-complete hexagonal structure (in two dimensions) or HCP packing (in three dimensions).

4.1.2 *Numerical values* We summarize the diagnostic values for the models and experimental granular networks in Appendix B. For each model, our results are means over all 1023 configurations that we generate to study the convergence characteristics of the diagnostics (see Section 4.1.1). For the experimental data, we take means over the 17 network realizations.

Based on the numbers in Tables B1 and B2 in Appendix B, we note several differences between our models. From the results, it is clear that the standard RGGs are the most unphysical of these models; we already made this point when visualizing associated particle systems. The proximity-modified RGGs have diagnostic values that resemble the experimental values more closely than the standard RGGs, and the force-modified RGGs generate the most realistic configurations. The diagnostic values for the modified-lattice model agree partly with those in the experimental data, but they are not better than the values for the force-modified RGGs, and the values of degree assortativity in the modified-lattice model differ significantly from those in the experimental configurations. The modified lattices are also visually rather different from the experimental packings, as noted in [13]. A closer look at the diagnostics of the bidisperse force-modified RGG reveals that it is the model that best matches the experimental data. This is also apparent from the distributions in Section 4.1.3 and Appendix C.

4.1.3 *Distributions of network characteristics* We now discuss the distributions of the network characteristics in ensembles of networks for the two-dimensional models and the experimental data. We show the distributions of the mean local clustering coefficient, transitivity, mean shortest-path length in the LCC, subgraph centrality, geodesic edge betweenness and communicability in Fig. 10. We show the distributions of the other measures in Appendix C. In each plot, the black curve is the distribution of the experimental data.

The top panels of Fig. 10 suggest that the mean local clustering coefficient and transitivity are useful measures for distinguishing between the unphysical and physical models. Specifically, the distributions of the standard RGGs do not overlap with the distributions from the other models, so we can clearly distinguish between the RGG distributions and those of the other models. A closer look at the distributions of mean local clustering coefficient and transitivity also reveals that the bidisperse force-modified RGG

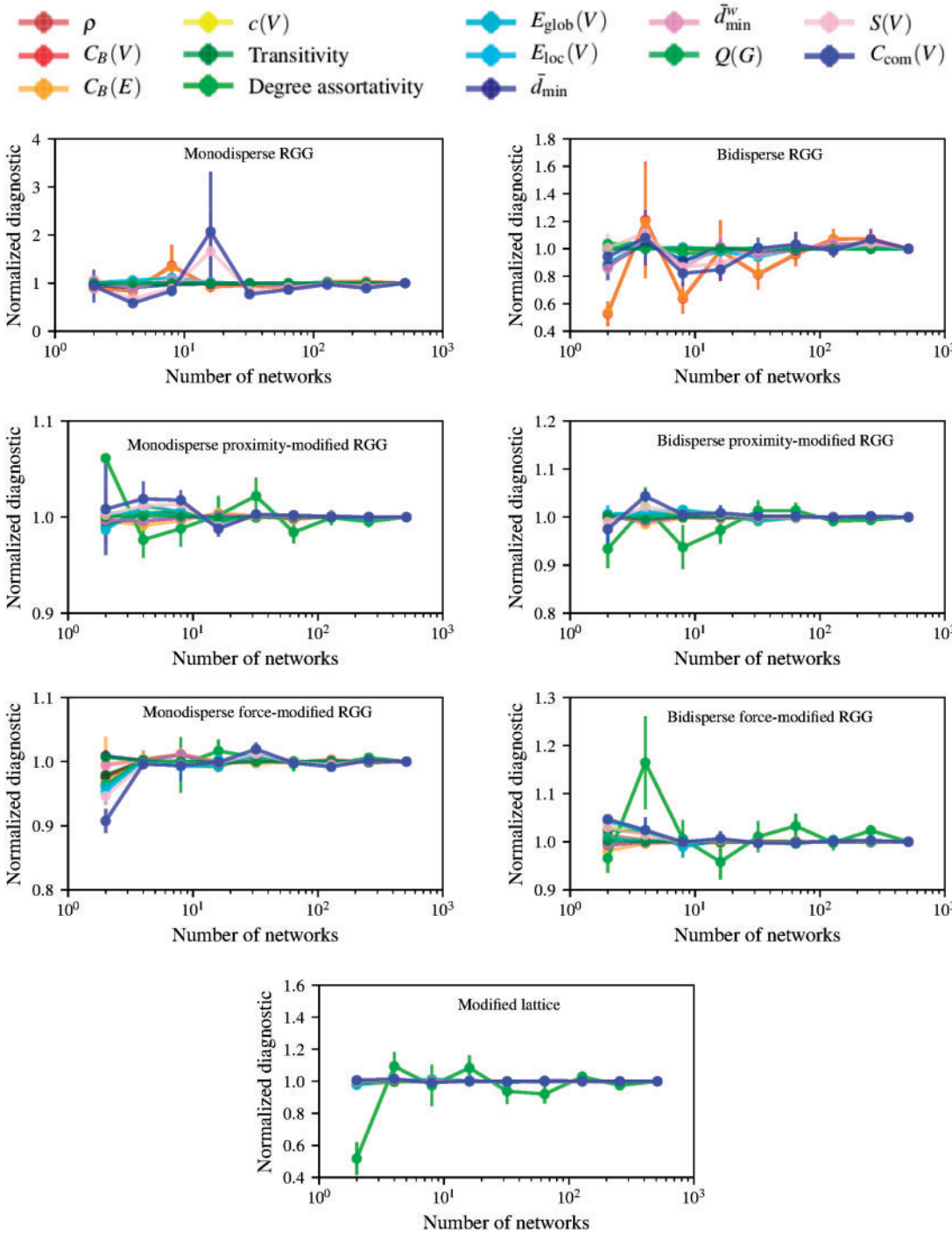

FIG. 9. Convergence characteristics of the network diagnostics. We show the mean diagnostic values and the corresponding error bars for ensembles with different numbers of networks. We normalize each diagnostic value by the mean that we compute from the largest ensemble of networks.

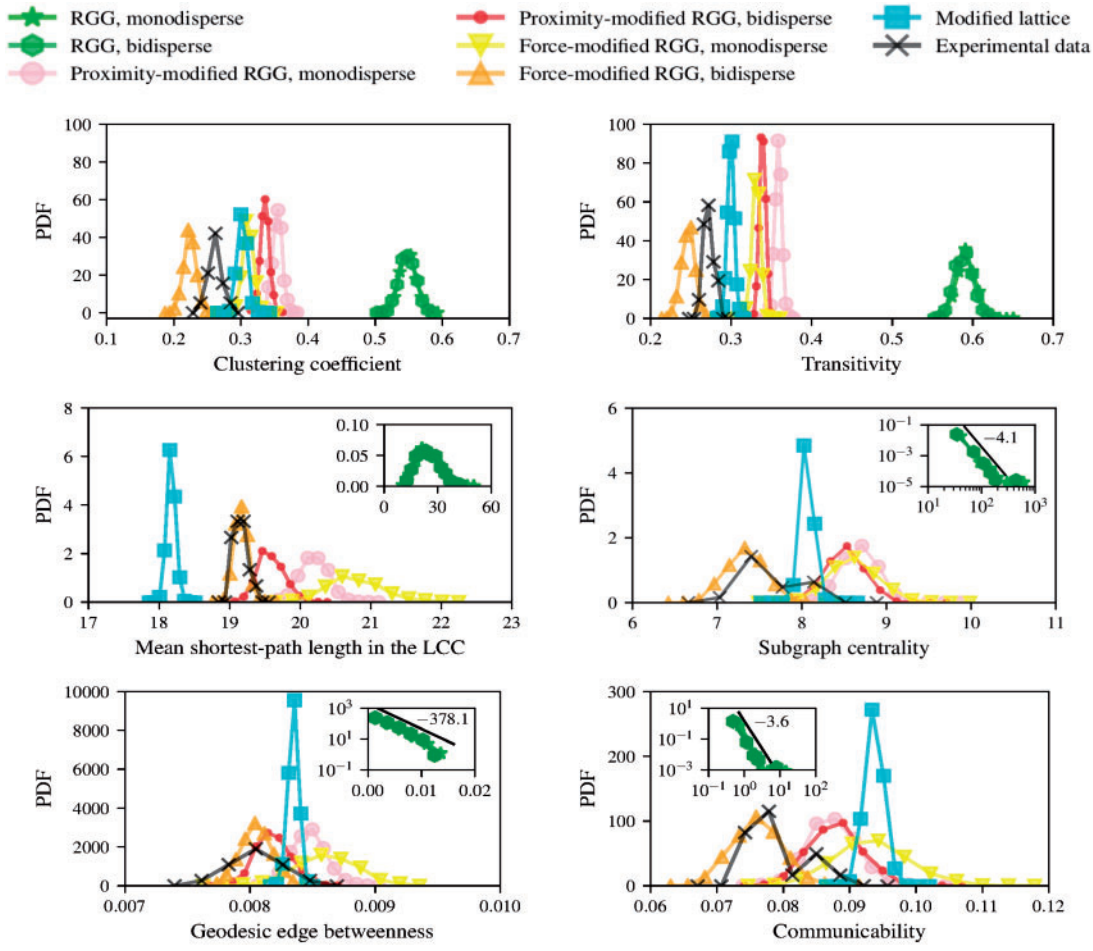

FIG. 10. Distributions of the diagnostics in the two-dimensional models and the experimental data. We show the distributions of the mean local clustering coefficient, transitivity, mean shortest-path length in the LCC, subgraph centrality, geodesic edge betweenness and communicability for the two-dimensional models and the experimental data. We compute these distributions from the 1023 network realizations for each model and the 17 realizations for the experimental data. The black lines in the insets are guides to the eye that are based on power-law and exponential fits (using the method of least squares) of distributions for standard bidisperse RGGs. (These insets also include the distributions for the standard monodisperse RGGs, but the fits use data only from the bidisperse RGGs.) The corresponding numbers indicate the slopes of these lines.

and the empirical granular networks have characteristics that are distinct from those of the other models. Based on these results, it is possible to distinguish these two network types from the proximity-modified RGGs and the monodisperse force-modified RGG. The modified-lattice distribution overlaps slightly with the one from the experimental data, although visual inspection of the networks indicates that these two types of networks are rather distinct from each other.

The distributions of the mean shortest-path length in the LCC in the experimental granular networks are similar to those that we obtain for the bidisperse force-modified RGG. By contrast, the distributions of the mean local clustering coefficient and transitivity in the experimental networks differ from those in

all of the models. This difference is extremely large for the unphysical models, but there is some overlap between experimental and model distributions for other models (e.g., more physical ones). Therefore, computing these quantities may not yield a clear distinction between experimental and model distributions when sampling from data.

In the remaining three panels of Fig. 10, we show the distributions of subgraph centrality, geodesic edge betweenness and communicability. In the corresponding insets, we show the distributions for the standard monodisperse and bidisperse RGG models, and we conclude that they differ qualitatively from the distributions of the corresponding diagnostics in the other models. We can connect this observation to the convergence characteristics of subgraph centrality, geodesic edge betweenness and communicability. To study these convergence characteristics, we compare the mean values of all diagnostics for different numbers of network realizations to the corresponding mean values in the largest ensemble (see Section 4.1.1). For subgraph centrality, geodesic edge betweenness and communicability in the unmodified RGGs, we observe larger deviations of the mean diagnostic values in the smaller ensembles from the mean values in the largest ensemble than is the case for the other diagnostics (see Fig. 9). This observation is also reflected by the qualitatively different distributions of those diagnostics (see Fig. 10).

4.2 *Diagnostics for three-dimensional granular networks*

We now briefly discuss the behaviour of the diagnostic distributions for the three-dimensional network models. We again focus on mean local clustering coefficient, transitivity, mean shortest-path length in the LCC, subgraph centrality, geodesic edge betweenness and communicability. We show the corresponding distributions in Fig. 11 and the remaining ones in Appendix C. For each model, we base the distributions on 256 network realizations.

In the top panels of Fig. 11, we show the distributions of mean local clustering coefficient and transitivity. As in our two-dimensional models, these two diagnostics distinguish successfully between physical and unphysical models of granular networks. The only major difference between our results in two and three dimensions are the distributions (which we show in the insets in some panels) in the modified-lattice model. In three dimensions, the mean local clustering coefficient and transitivity values for this model are to the left of the bidisperse force-modified RGG model.

For mean shortest-path length in the LCC, we observe that, in contrast to our observations in two dimensions, the distribution of the bidisperse proximity-modified RGG is to the left of the bidisperse force-modified RGG. Moreover, the distributions of the monodisperse and bidisperse force-modified RGGs and the monodisperse proximity-modified RGG overlap more in three dimensions than in two dimensions. We also observe these differences between two and three dimensions in the distributions of geodesic edge betweenness. The distributions of subgraph centrality and communicability in three dimensions are qualitatively more similar to the ones in two dimensions than is the case for the other network diagnostics.

5. Conclusions and discussion

We described and computed several common network diagnostics for a variety of two-dimensional and three-dimensional models of granular networks, ranging from unphysical ones with overlapping particles to physical ones that are free (or at least mostly free) of overlaps. We studied the convergence properties of the diagnostics to identify a reasonable number of network realizations for the computation of the diagnostic distributions.

We examined the ability of the various network diagnostics to distinguish between physical and unphysical models of granular networks in two and three dimensions. Our results suggest that mean local clustering coefficient and transitivity, which are related measures of triadic closure, are appropriate

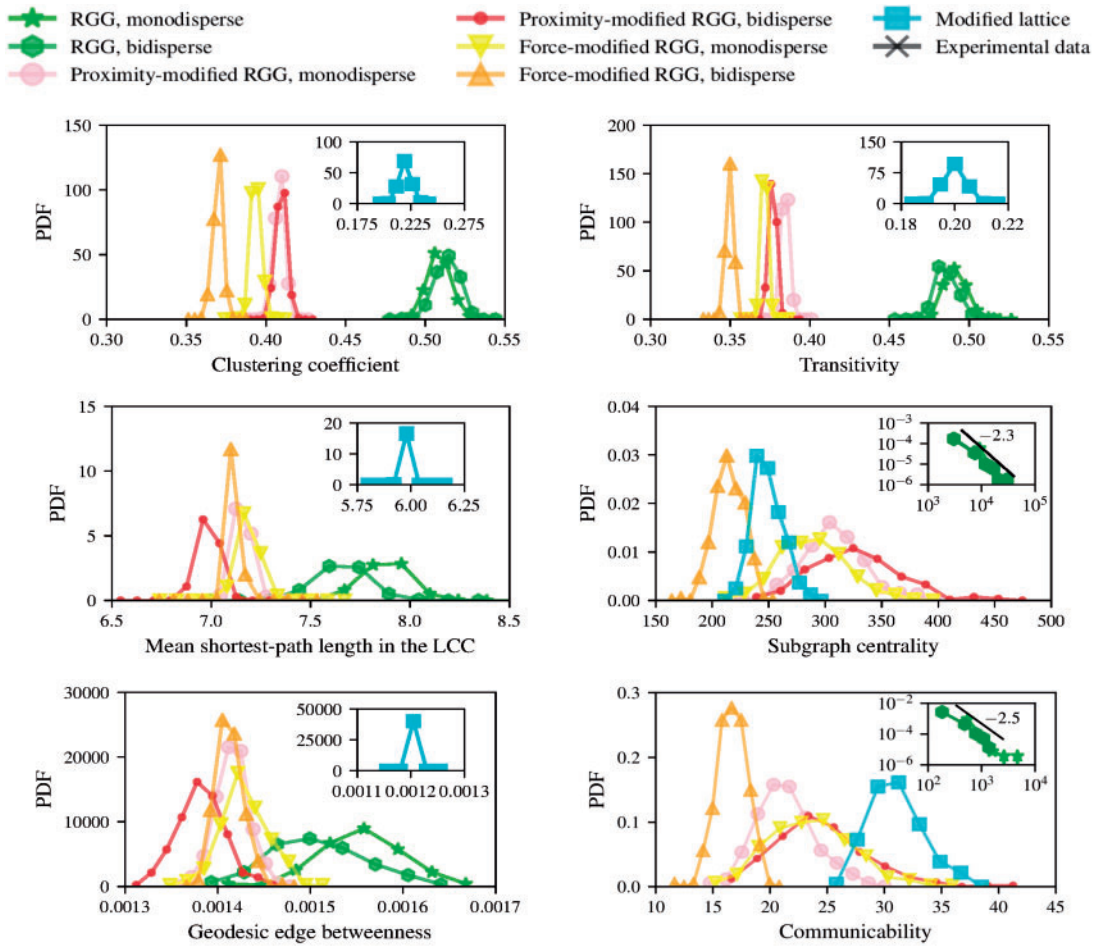

FIG. 11. Distributions of the diagnostics in three-dimensional networks. We show the distributions of the mean local clustering coefficient, transitivity, mean shortest-path length in the LCC, subgraph centrality, geodesic edge betweenness and communicability for the three-dimensional network models. We base the distributions on 256 network realizations for each model. The black lines in the insets are guides to the eye that we obtain from power-law fits (using the method of least squares) of the distributions for standard bidisperse RGGs. (These insets also include the distributions for the standard monodisperse RGGs, but the fits use data only from the bidisperse RGGs.) The corresponding numbers indicate the slopes of these lines. In some panels, we show the distribution for the modified-lattice model in an inset.

diagnostics to distinguish between the physical and unphysical models. The power of these two measures lies in the fact that their distributions for the different models are readily distinguishable from each other. In some cases, the diagnostics distributions of the two-dimensional and three-dimensional networks appear to satisfy markedly different statistical distributions, a phenomenon that we also expect to observe in comparisons of two-dimensional and three-dimensional granular networks from experiments.

Our results advance spatial random-graph models of granular networks and illustrate that simple modifications of random geometric graphs that incorporate a minimal amount of physics are useful models for gaining insights into granular and particulate networks. In future studies, it will be useful to investigate the effects of shape variations, such as by examining the effects of different rectangular box geometries [30] and irregular boundaries [31] on network diagnostics in spatial random-graph models.

Acknowledgements

We thank Karen E. Daniels for providing the experimental granular network data from [29]. We also thank David Kammer for the use of his cluster computing infrastructure and Kornel Kovacs for cluster maintenance.

References

1. Berthier, E., Porter, M. A. & Daniels, K. E. (2019) Forecasting failure locations in 2-dimensional disordered lattices. *Proc. Natl. Acad. Sci. USA*, **116**, 16742–16749.
2. Papadopoulos, L., Porter, M. A., Daniels, K. E. & Bassett, D. S. (2018) Network analysis of particles and grains. *J. Complex Netw.*, **6**, 485–565.
3. Smart, A. & Ottino, J. M. (2008) Granular matter and networks: Three related examples. *Soft Matter*, **4**, 2125–2131.
4. Smart, A., Umbanhowar, P. & Ottino, J. (2007) Effects of self-organization on transport in granular matter: A network-based approach. *Europhys. Lett.*, **79**, 24002.
5. Anderson, T. L. (2017) *Fracture Mechanics: Fundamentals and Applications*. Boca Raton, FL: CRC Press.
6. Heisser, R. H., Patil, V. P., Stoop, N., Villermaux, E. & Dunkel, J. (2018) Controlling fracture cascades through twisting and quenching. *Proc. Natl. Acad. Sci. USA*, **115**, 8665–8670.
7. Herrmann, H. J. & Roux, S. (2014) *Statistical Models for the Fracture of Disordered Media*. Amsterdam, The Netherlands: Elsevier.
8. Cates, M. E., Wittmer, J. P., Bouchaud, J.-P. & Claudin, P. (1999) Jamming and static stress transmission in granular materials. *Chaos*, **9**, 511–522.
9. Andreotti, B., Forterre, Y. & Pouliquen O. (2013) *Granular Media: Between Solid and Fluid*. Cambridge, UK: Cambridge University Press.
10. Jaeger, H. M., Nagel, S. R. & Behringer, R. P. (1996) Granular solids, liquids, and gases. *Rev. Mod. Phys.*, **68**, 1259–1273.
11. Bassett, D. S., Owens, E. T., Porter, M. A., Manning, M. L. & Daniels, K. E. (2015) Extraction of force-chain network architecture in granular materials using community detection. *Soft Matter*, **11**, 2731–2744.
12. Barthelemy, M. (2018) *Morphogenesis of Spatial Networks*. Cham, Switzerland: Springer International Publishing.
13. Setford, J. (2014) Models of granular networks in two and three dimensions. Undergraduate thesis, Department of Physics, University of Oxford. Available at: https://www.math.ucla.edu/~mason/research/setford-final.pdf.
14. Coon, J., Dettmann, C. P. & Georgiou, O. (2012) Impact of boundaries on fully connected random geometric networks. *Phys. Rev. E*, **85**, 011138.
15. Dettmann, C. P. & Georgiou, O. (2016) Random geometric graphs with general connection functions. *Phys. Rev. E*, **93**, 032313.
16. Newman, M. E. J. (2018) *Networks*, 2nd edn. Oxford, UK: Oxford University Press.
17. Hagberg, A., Schult, D. & Swart, P. (2019) NetworkX. Available at: https://networkx.github.io/documentation/stable/index.html (last accessed 19 September 2019).
18. Girvan, M. & Newman, M. E. J. (2002) Community structure in social and biological networks. *Proc. Nat. Acad. Sci. USA*, **99**, 7821–7826.
19. Newman, M. E. J. (2003) Mixing patterns in networks. *Phys. Rev. E*, **67**, 026126.
20. Latora, V. & Marchiori, M. (2001) Efficient behavior of small-world networks. *Phys. Rev. Lett.*, **87**, 198701.
21. Fortunato, S. & Hric, D. (2016) Community detection in networks: A user guide. *Phys. Rep.*, **659**, 1–44.
22. Porter, M. A., Onnela, J.-P. & Mucha, P. J. (2009) Communities in networks. *Notices Am. Math. Soc.*, **56**, 1082–1097, 1164–1166.
23. Blondel, V. D., Guillaume, J.-L., Lambiotte, R. & Lefebvre, E. (2008) Fast unfolding of communities in large networks. *J. Stat. Mech.*, **2008**, P10008.
24. Estrada, E. & Rodríguez-Velázquez, J. A. (2005) Subgraph centrality in complex networks. *Phys. Rev. E*, **71**, 056103.

25. Estrada, E. & Hatano, N. (2008) Communicability in complex networks. *Phys. Rev. E*, **77**, 036111.
26. Owens, E. T. & Daniels, K. E. (2011) Sound propagation and force chains in granular materials. *Europhys. Lett.*, **94**, 54005.
27. Chong, C., Porter, M. A., Kevrekidis, P. G. & Daraio, C. (2017) Nonlinear coherent structures in granular crystals. *J. Phys. Condens. Matter*, **29**, 413003.
28. Behringer, R. P. & Chakraborty, B. (2018) The physics of jamming for granular materials: A review. *Rep. Prog. Phys.*, **82**, 012601.
29. Bassett, D. S., Owens, E. T., Daniels, K. E. & Porter, M. A. (2012) Influence of network topology on sound propagation in granular materials. *Phys. Rev. E*, **86**, 041306.
30. Estrada, E. & Sheerin, M. (2015) Random rectangular graphs. *Phys. Rev. E*, **91**, 042805.
31. Dettmann, C. P., Georgiou, O. & Coon, J. P. (2015) More is less: Connectivity in fractal regions. *2015 International Symposium on Wireless Communication Systems (ISWCS)*. Piscataway, New Jersey, USA: IEEE, pp. 636–640.

Appendix

A. Force-modified configurations

To obtain the potential-energy thresholds V^* (below which we no longer update particle positions) in Section 3.3, we consider the first term of Eq. (23) and set the distance between two neighbouring particles, k and l, to be $r_k/200$ (which depends only on one of the particles). In a monodisperse packing, we use $r_k = r$, whereas $r_k \in \{r_1, r_2\}$ in bidisperse packings. For simplicity, we consider the case in which every particle has 6 neighbours. In a monodisperse packing, we use 1122 particles of radius $r = 4.5$ mm to determine a value of the potential-energy threshold. In a bidisperse packing, we consider a system with 561 particles of radius $r_1 = 4.5$ mm and 561 with radius $r_2 = 5.5$ mm.

Supposing that the radii are unitless, the potential-energy thresholds are

$$\begin{aligned} V^*_{\text{mono}} &= \sum_k \sum_{l \neq k} \left[\frac{1}{2}(r_k + r_l) - \frac{1}{2}|\mathbf{x}_k - \mathbf{x}_l| \right]_+^{\beta+1} \\ &= \sum_k 6 \times \left(\frac{r_k}{200} \right)^{\beta+1} = 1122 \times 6 \times \left(\frac{4.5}{200} \right)^{1.5} \\ &\approx 22.7 \end{aligned} \tag{A.1}$$

for the monodisperse packing and

$$\begin{aligned} V^*_{\text{bi}} &= \sum_k \sum_{l \neq k} \left[\frac{1}{2}(r_k + r_l) - \frac{1}{2}|\mathbf{x}_k - \mathbf{x}_l| \right]_+^{\beta+1} \\ &= \sum_k 6 \times \left(\frac{r_k}{200} \right)^{\beta+1} = 561 \times 6 \times \left(\frac{4.5}{200} \right)^{1.5} + 561 \times 6 \times \left(\frac{5.5}{200} \right)^{1.5} \\ &\approx 26.7 \end{aligned} \tag{A.2}$$

for the bidisperse packing. In both cases, we set $\beta = 1/2$, which is the value that we used for our computations in Section 3. These two values of the potential-energy threshold provide an estimate to assess the quality of network configurations that we generate using force-modified RGG models. For

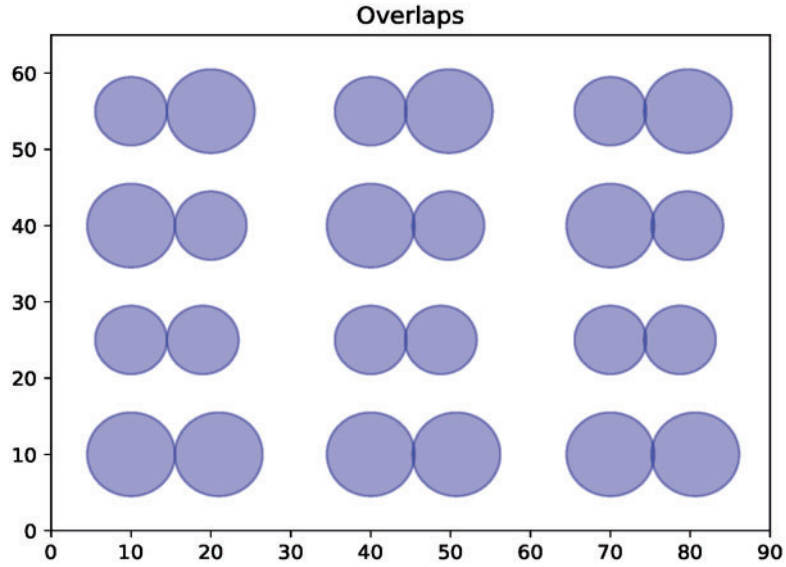

FIG. A1. Overlapping particles. The left column shows particles with an overlap of $r_k/200$, where k indicates the particle on the left. In the middle column, the overlap is $r_k/20$. In the right column, it is $r_k/15$.

three-dimensional models, we take the number of neighbours of a particle to be 12. Therefore, the thresholds in three dimensions are $V^*_{\text{mono}} \approx 45.4$ and $V^*_{\text{bi}} \approx 53.4$.

We also examine the maximum overlap of our configurations. Based on visual inspection of Fig. A1, we conclude that an overlap of $r_k/200$ is sufficiently small. By contrast, overlap distances of $r_k/20$ and $r_k/15$ are visible.

B. Diagnostic values

We present our numerical results for the diagnostics of the various models in Tables B1 and B2.

TABLE B1 *Network diagnostics of the experimental data, the two-dimensional modified-lattice model, and the two-dimensional RGGs. We average the results over* 17 *realizations for the experimental data and over* 1023 *realizations for the random-graph models*

	Experimental data		Modified lattice	
Diagnostic	Mean	Standard deviation	Mean	Standard deviation
Edge density	0.0038	$< 10^{-4}$	0.0042	$< 10^{-4}$
Geodesic node betweenness	0.0163	0.0002	0.0168	0.0001
Geodesic edge betweenness	0.0080	0.0002	0.0083	$< 10^{-4}$
Mean local clustering coefficient	0.2613	0.0100	0.3019	0.0068
Transitivity	0.2714	0.0070	0.2994	0.0042
Degree assortativity	0.1377	0.0236	0.0648	0.0262
Global efficiency	0.0772	0.0005	0.0812	0.0003
Local efficiency	0.3301	0.0156	0.3886	0.0089
Mean shortest-path length in the LCC	19.1634	0.1069	18.1703	0.0585
Weighted mean shortest-path length	19.1483	0.1046	18.1456	0.0680
Maximized modularity	0.8712	0.0045	0.8487	0.0028
Subgraph centrality	7.6236	0.2958	8.0579	0.0678
Communicability	0.0790	0.0046	0.0937	0.0013
	RGG (monodisperse)		RGG (bidisperse)	
Diagnostic	Mean	Standard deviation	Mean	Standard deviation
Edge density	0.0038	$< 10^{-4}$	0.0038	$< 10^{-4}$
Geodesic node betweenness	0.0057	0.0046	0.0059	0.0046
Geodesic edge betweenness	0.0028	0.0022	0.0029	0.0022
Mean local clustering coefficient	0.5485	0.0126	0.5480	0.0121
Transitivity	0.5921	0.0119	0.5885	0.0113
Degree assortativity	0.5839	0.0398	0.5581	0.0409
Global efficiency	0.0225	0.0045	0.0232	0.0047
Local efficiency	0.6314	0.0128	0.6304	0.0127
Mean shortest-path length in the LCC	24.6106	6.4311	24.4985	6.2803
Weighted mean shortest-path length	15.9323	5.2432	15.9851	5.1460
Maximized modularity	0.9528	0.0032	0.9521	0.0033
Subgraph centrality	35.0580	29.4708	34.9849	19.7010
Communicability	0.4376	0.6047	0.4336	0.3419

C. Additional diagnostic distributions

In Figs. C1 and C2, we show the distributions of the diagnostics that we did not show in Section 4.

TABLE B2 *Network diagnostics of the two-dimensional proximity-modified RGGs and the two-dimensional force-modified RGGs. We average the results over* 1023 *realizations*

	Proximity-modified RGG (mono)		Proximity-modified RGG (bi)	
Diagnostic	Mean	Standard deviation	Mean	Standard deviation
Edge density	0.0038	$< 10^{-4}$	0.0038	$< 10^{-4}$
Geodesic node betweenness	0.0171	0.0002	0.0166	0.0002
Geodesic edge betweenness	0.0085	0.0001	0.0082	0.0001
Mean local clustering coefficient	0.3540	0.0070	0.3356	0.0066
Transitivity	0.3584	0.0044	0.3389	0.0040
Degree assortativity	0.2799	0.0270	0.2179	0.0268
Global efficiency	0.0734	0.0006	0.0754	0.0006
Local efficiency	0.4663	0.0100	0.4430	0.0099
Mean shortest-path length in the LCC	20.1977	0.1987	19.5844	0.1852
Weighted mean shortest-path length	20.1808	0.2012	19.5716	0.1858
Maximized modularity	0.8754	0.0031	0.8670	0.0032
Subgraph centrality	8.6839	0.2133	8.5141	0.2257
Communicability	0.0874	0.0036	0.0879	0.0040
	Force-modified RGG (mono)		Force-modified RGG (bi)	
Diagnostic	Mean	Standard deviation	Mean	Standard deviation
Edge density	0.0038	$< 10^{-4}$	0.0038	$< 10^{-4}$
Geodesic node betweenness	0.0175	0.0004	0.0162	0.0001
Geodesic edge betweenness	0.0086	0.0002	0.0081	0.0001
Mean local clustering coefficient	0.3106	0.0076	0.2238	0.0089
Transitivity	0.3311	0.0050	0.2463	0.0080
Degree assortativity	0.4404	0.0357	0.1952	0.0370
Global efficiency	0.0717	0.0010	0.0774	0.0004
Local efficiency	0.4172	0.0123	0.2789	0.0137
Mean shortest-path length in the LCC	20.7794	0.3931	19.1593	0.0938
Weighted mean shortest-path length	20.6838	0.4227	19.1463	0.0968
Maximized modularity	0.8659	0.0043	0.8410	0.0023
Subgraph centrality	8.6134	0.2818	7.3340	0.2270
Communicability	0.0934	0.0055	0.0760	0.0037

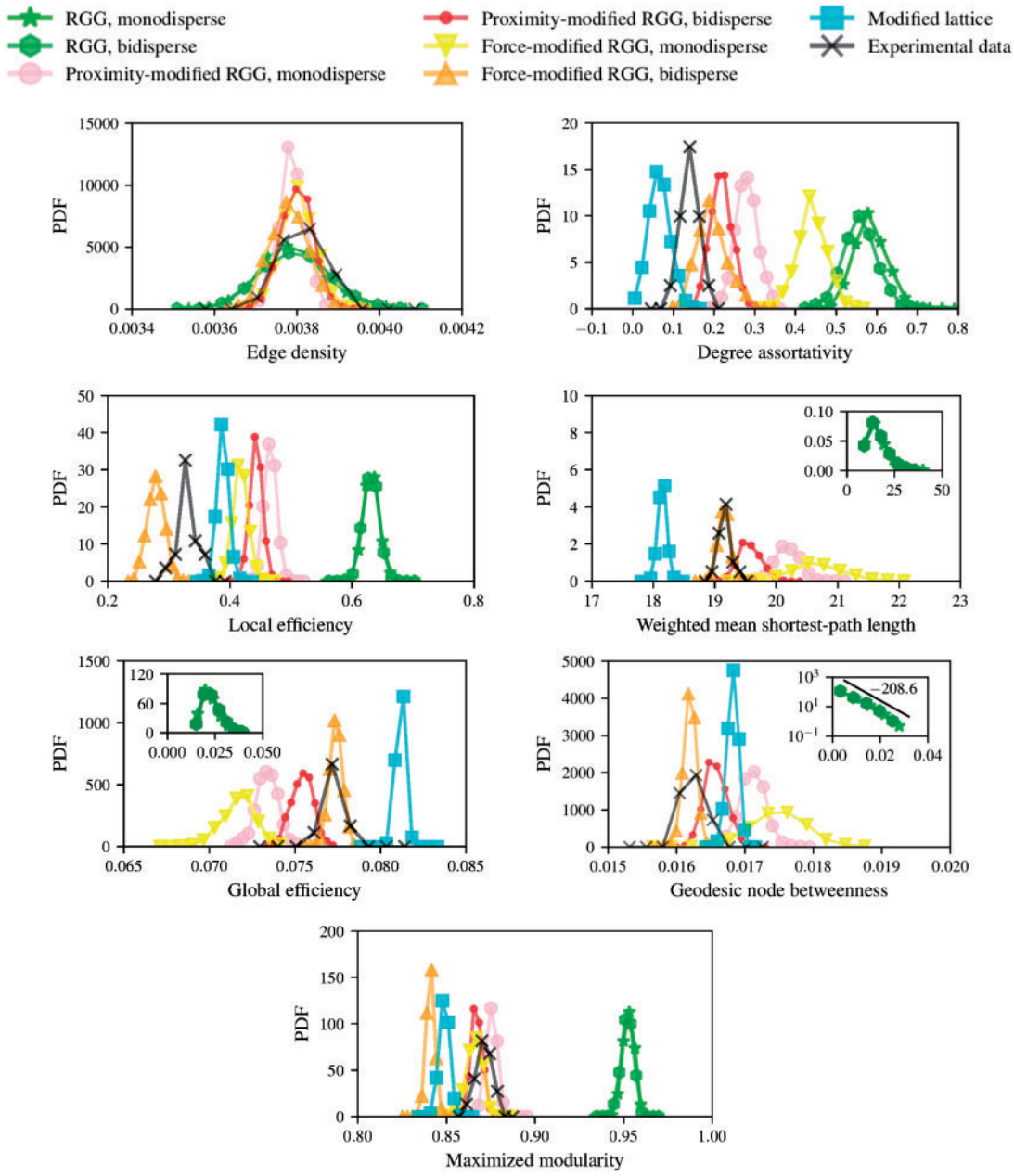

FIG. C1. Distributions of the remaining diagnostics in the two-dimensional models and experimental data. We show the distributions of edge density, degree assortativity, local efficiency, weighted mean shortest-path length, global efficiency, geodesic node betweenness and maximized modularity for the two-dimensional models and the experimental data. We determine the distributions from 1023 network realizations for each model and for 17 realizations for the experimental data. In the plot of the edge-density distribution, we do not show the distribution of the modified-lattice model, because the edge density for this model always has exactly the same value. The black line in the inset of the plot of geodesic node betweenness is a guide to the eye that we obtain from a power-law fit (using the method of least squares) of the distributions for standard bidisperse RGGs. (These insets also include the distributions for the standard monodisperse RGGs, but the fits use data only from the bidisperse RGGs.) The corresponding number indicates the slope of this line.

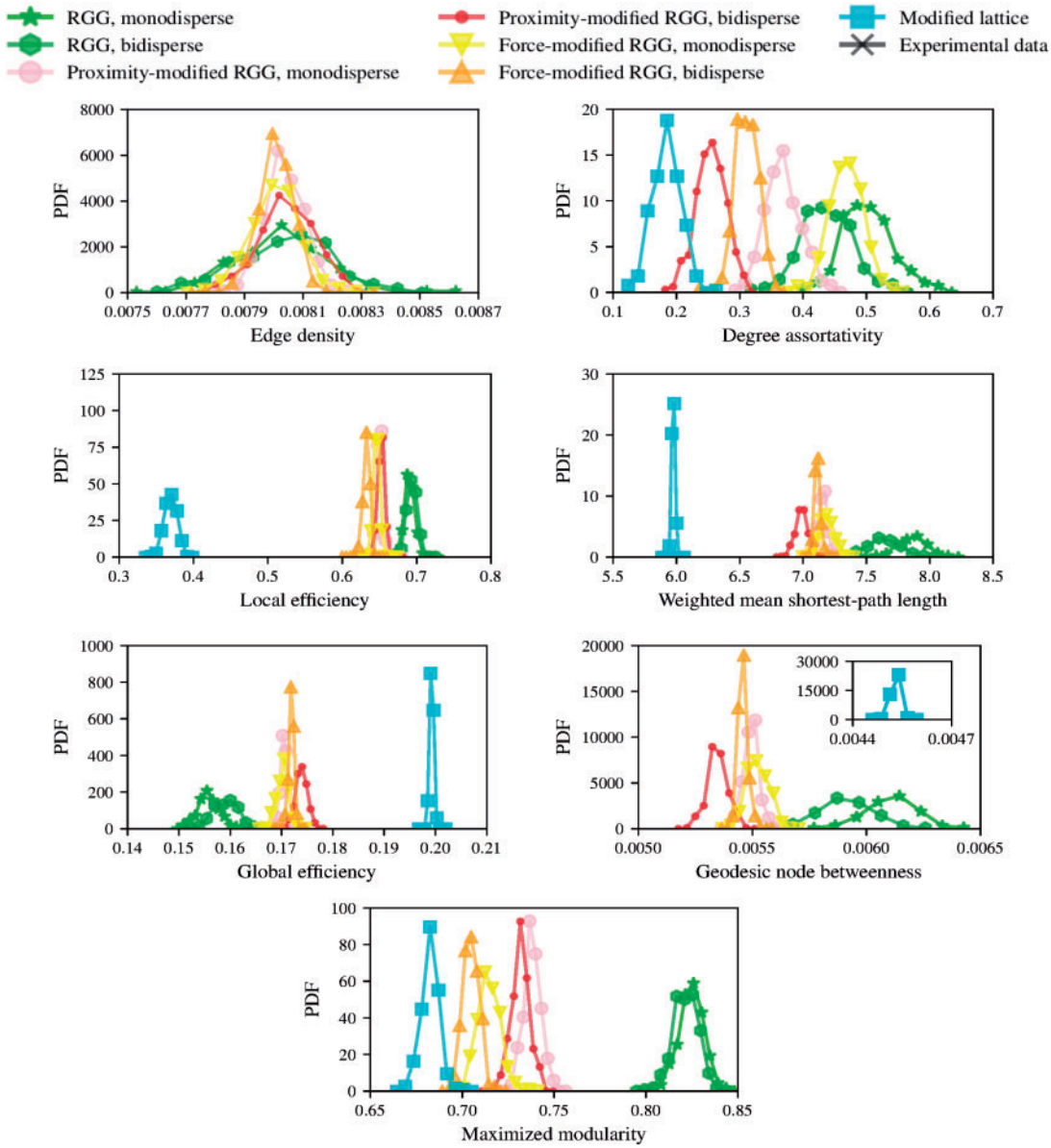

FIG. C2. Distributions of the remaining diagnostics in the three-dimensional models. We show the distributions of edge density, degree assortativity, local efficiency, weighted mean shortest-path distance, global efficiency, geodesic node betweenness and maximized modularity for the three-dimensional models. We determine the distributions from 256 network realizations for each model. In the plot of the edge-density distribution, we do not show the distribution of the modified-lattice model, because the edge density for this model always has exactly the same value. For geodesic node betweenness, we show the distribution for the modified-lattice model in the inset.